

A Dynamic Approach to Quantitative Precipitation Estimation Using Multiradar Multigauge Network

Yabin Gou, Haonan Chen[✉], *Member, IEEE*, and V. Chandrasekar, *Fellow, IEEE*

Abstract—Effective utilization of the changing precipitation microphysics in real-time radar quantitative precipitation estimation (QPE) is challenging, which requires dynamic adjustment of the radar reflectivity (Z) and rain rate (R) relations. This article develops and demonstrates two dynamic radar rainfall approaches using 16 Doppler weather radars and 4579 surface rain gauges deployed over the Eastern Jiang Huai River Basin (EJRB) in China. Both approaches are derived based on the radar-gauge feedback mechanism. Although the Z – R relations in both approaches are dynamically adjusted within a precipitation system, one is using a single global optimum (SGO) Z – R relation, while the other is using different Z – R relations for different storm cells identified by a storm cell identification and tracking (SCIT) algorithm. Four precipitation events featured by different rainfall characteristics are investigated to evaluate the performances of various QPE methodologies. In addition, the short-term vertical profile of reflectivity (VPR) clusters is extensively analyzed to resolve the storm-scale characteristics of different storm cells. The evaluation results based on independent gauge observations show that both rainfall approaches with dynamic Z – R relations perform much better than the fixed Z – R relations. The adaptive approach incorporating the SCIT algorithm and real-time gauge measurements has the best performance since it can better capture the spatial variability and evolution of precipitation.

Index Terms—Dynamic approach, quantitative precipitation estimation (QPE), storm cell identification and tracking (SCIT), weather radar.

I. INTRODUCTION

RADAR-BASED quantitative precipitation estimation (QPE) at high spatiotemporal resolution is critical for severe weather warning and urban flash flood forecast [1], [2].

Manuscript received July 22, 2019; revised November 21, 2019 and January 28, 2020; accepted February 21, 2020. Date of publication March 10, 2020; date of current version August 28, 2020. This work was supported in part by the National Natural Science Foundation of China (NSFC) under Grant 41705018 and Grant 41575036. The work of Yabin Gou was supported in part by the Zhejiang Provincial Natural Science Fund under Award LY17D050001 and in part by Zhejiang Major Science and Technology Special Projects under Award 2017C03035. The work of Haonan Chen was supported by the California Department of Water Resources (DWR) and the Physical Sciences Division (PSD) at the National Oceanic and Atmospheric Administration's (NOAA) Earth System Research Laboratory. (*Corresponding author: Haonan Chen.*)

Yabin Gou is with the Hangzhou Meteorological Bureau, Hangzhou 310051, China, and also with the Zhejiang Institute of Meteorological Sciences, Hangzhou 310021, China.

Haonan Chen is with the Physical Sciences Division (PSD), Earth System Research Laboratory, NOAA, Boulder, CO 80305 USA, and also with the Cooperative Institute for Research in the Atmosphere (CIRA), Fort Collins, CO 80523 USA (e-mail: haonan.chen@colostate.edu).

V. Chandrasekar is with the Department of Electrical and Computer Engineering, Colorado State University, Fort Collins, CO 80523 USA.

Color versions of one or more of the figures in this article are available online at <http://ieeexplore.ieee.org>.

Digital Object Identifier 10.1109/TGRS.2020.2976724

Although many operational weather radars such as the United States Weather Surveillance Radar-1988 Doppler (WSR-88D) systems have been upgraded with dual-polarization capability, single-polarized radars still form the cornerstones of national weather forecasting infrastructure in many countries. As such, there is a continuing interest in the radar reflectivity-based rainfall estimation methodologies.

In general, the climatology-based radar QPE algorithm is utilized, which attempts to obtain the optimal radar reflectivity (Z) and rain rate (R) relationships based on long-term radar reflectivity and surface gauge and/or disdrometer measurements [3]. In addition, it is commonly recognized that a single Z – R relation is not sufficient to represent local rainfall microphysics in different precipitation events, even in different rainfall regimes within a single storm system. Significant progress has been achieved to address radar QPE over recent years. For example, the WSR-88D radars adopt different Z – R relations for different rainfall types [4]. In particular, $Z = 200R^{1.6}$, $Z = 300R^{1.4}$ and $Z = 230R^{1.53}$ are respectively applied for stratiform, convective, and tropical rain. Similarly, the multiradar multisensor (MRMS) system calculates the surface precipitation rate using multiple Z – R relations for different precipitation types, namely, warm and cold stratiform rain, convective rain and hail, and snow [5]. However, the nonuniformly distributed precipitation at different regimes is still difficult to be characterized, especially in mountainous terrain where orographic enhancement, partial beam blockage (PBB), and bright band (BB) contamination are prevalent [6]–[9]. Even if the radar data is not affected by system calibration, ground clutter, and/or PBB, appropriate processing is required to create regular reflectivity grids that can capture the evolution of precipitation. In addition, dynamic Z – R relationships are necessary to differentiate the spatiotemporal variability of precipitation for QPE applications [10]–[12].

Alfieri *et al.* [13] proposed a single globally optimal (SGO) approach for producing accurate radar-based rainfall estimates by adjusting the coefficients in the Z – R relations continuously in time. Although this SGO-based approach showed reasonable performance for the 19 rainfall events presented in their article, the spatial variability of precipitation still cannot be reflected in their adaptive algorithm. Gou *et al.* [14], [15] developed an improved radar rainfall approach based on reflectivity threshold and the storm cell identification and tracking (SCIT) algorithm described in [16]. In this improved method, the storm-scale precipitation microphysics are derived from the multiradar hybrid mosaic reflectivity (MHMR) field, and more representative Z – R relationships are applied for individual rainstorm cells. Preliminary application over the

eastern Tibetan Plateau showed the great potential of this dynamic rainfall methodology. In this article, we extend the study in [15] to a more challenging scenario. The main goal is to demonstrate the performance of the physically based dynamic radar rainfall system (hereafter referred to as the SCIT-based approach since it belongs to the same category with the method in [15]) during large-scale severe convective storm events. This article is also motivated by the fact that more than 60 000 ground weather stations have been deployed in China, which serve as another important source for routine weather monitoring and precipitation measurement. Each station is equipped with a rain gauge. Such a dense gauge network enables real-time feedback to radar rainfall algorithms over a large domain. In addition, the most important synoptic signatures during flood season in China are influenced by the East Asian Monsoon (or Meiyu front). Large-scale severe convective precipitation systems, even typhoons, often occur during the flood seasons, which usually include multiple precipitation regimes characterized by high spatial variability.

This article is organized as follows. Section II describes the radar data processing and QPE algorithms; Section III presents an application study in the Eastern Jiang Huai River Basin (EJRB) of China; quantitative evaluation of different radar QPE approaches is detailed in Section IV; Section V summarizes the main findings of this article.

II. METHODOLOGIES

A. Radar Data Processing

The dynamic radar rainfall estimation mechanism is devised to work on the MHMR field. Therefore, radar reflectivity data quality control and mosaicking should be conducted prior to the implementation of adaptive radar rainfall relations. Here, three data preprocessing steps are highlighted to ensure reliable radar QPE in the application study detailed in Sections III and IV.

- 1) *Ground Clutter Filtering and Clear Air Echo Identification*: It is well known that ground clutters, which are typically featured with static positions, are often embedded in the precipitation observations. The fuzzy logic approach described by Berenguer *et al.* [17] is implemented in this article in order to eliminate the clutters and associated anomalous propagation effects. In addition, this article incorporates the vertical gradient of reflectivity, the standard deviation of radial velocity, as well as the radar echo top (i.e., reflectivity threshold of 20 dBZ) to discriminate clear air echoes.
- 2) *Beam Obstruction Consideration*: The PBB ratio of each radar's radial profile is calculated and the sampling volumes are removed if the PBB ratio is higher than 50%. The reflectivity profiles are corrected if the PBB ratio is small, based on the approaches in [4] and [18].
- 3) *Constructing the MHMR Field*: With the temporally matched reflectivity data from individual radars, the MHMR field can be constructed. In this article, the nearest neighbor approach is utilized to map the multiradar observations on regular Cartesian grids at a horizontal resolution of $0.005^\circ \times 0.005^\circ$ latitude/longitude coordinates.

B. Dynamic Radar Rainfall Algorithm

Fig. 1 shows the system diagram of the SGO- and SCIT-based radar QPE algorithms. Both methods utilize the radar estimate and gauge measurement pairs $[R_i, G_i]$ to provide feedback information to the selection of Z - R relations. Here, it should be noted that R_i and G_i represent the radar-derived 6-min (volume scan time) rainfall amount and corresponding gauge measurement, respectively. R_i is derived by averaging two temporally adjacent radar rainfall estimates from the MHMR field. The parameters A and b in $Z = AR^b$ are dynamically fit every 6 min through the optimization equation defined as

$$\delta = \min \sum_{i=1}^n [(G_i - R_i)^2 + |G_i - R_i|] \quad (1)$$

where i denotes the gauge index; n is the total number of valid gauges used in the optimization process. Equation (1) is a quadratic function, and the first term on the right-hand side will increase quickly and dominate if the difference between G_i and R_i is higher than 1 mm. Otherwise, the second term will contribute more to the difference. After obtaining the optimal Z - R relation at each time frame with the standard weighted least squares method, hourly rainfall accumulations are derived for each grid pixel using the 6-min estimates. As shown in Fig. 1, both the SGO- and SCIT-based algorithms rely on the gauge-radar pairs. Ensuring the gauge data quality is critical to the derivation of optimal Z - R relations. In real-time operational applications, the gauge data quality control process described in Fig. 1 is adopted to disregard suspicious records.

The main difference between the SGO- and SCIT-based approaches is that the SGO-based algorithm only derives one global Z - R relation using all the radar-gauge pairs. The local variability in the spatial distribution of precipitation is not taken into account. Instead, the SCIT-based approach incorporates a reflectivity partitioning process to better capture the precipitation variability within a storm system. In particular, a reflectivity threshold of 20 dBZ is applied to the MHMR field first. The relation of $Z = 200R^{1.6}$ is used by default if the radar reflectivity is less than 20 dBZ. In the regions where the reflectivity is higher than 20 dBZ, a 5-dBZ step is applied to further refine the reflectivity field into different areas. As a result, the precipitation system is dynamically classified as multiple storm cells. The optimization process in (1) is implemented for each identified cell to derive appropriate Z - R relationships. For comparison purposes, the convective rainfall relation $Z = 300R^{1.4}$, the Marshall-Palmer relationship $Z = 200R^{1.6}$, as well as the tropical rainfall relation $Z = 230R^{1.25}$ are also implemented for the same radar reflectivity field. Five hourly rainfall estimates derived from the same radar data set are verified and evaluated using independent rain gauge observations.

In addition, the vertical profile of reflectivity (VPR) of each storm cell is derived based on the 3-D multiradar reflectivity mosaic field. The reflectivity mosaic is constructed from temporally matched single radar reflectivity grids using the nearest neighbor approach [5]. The averaged reflectivity at

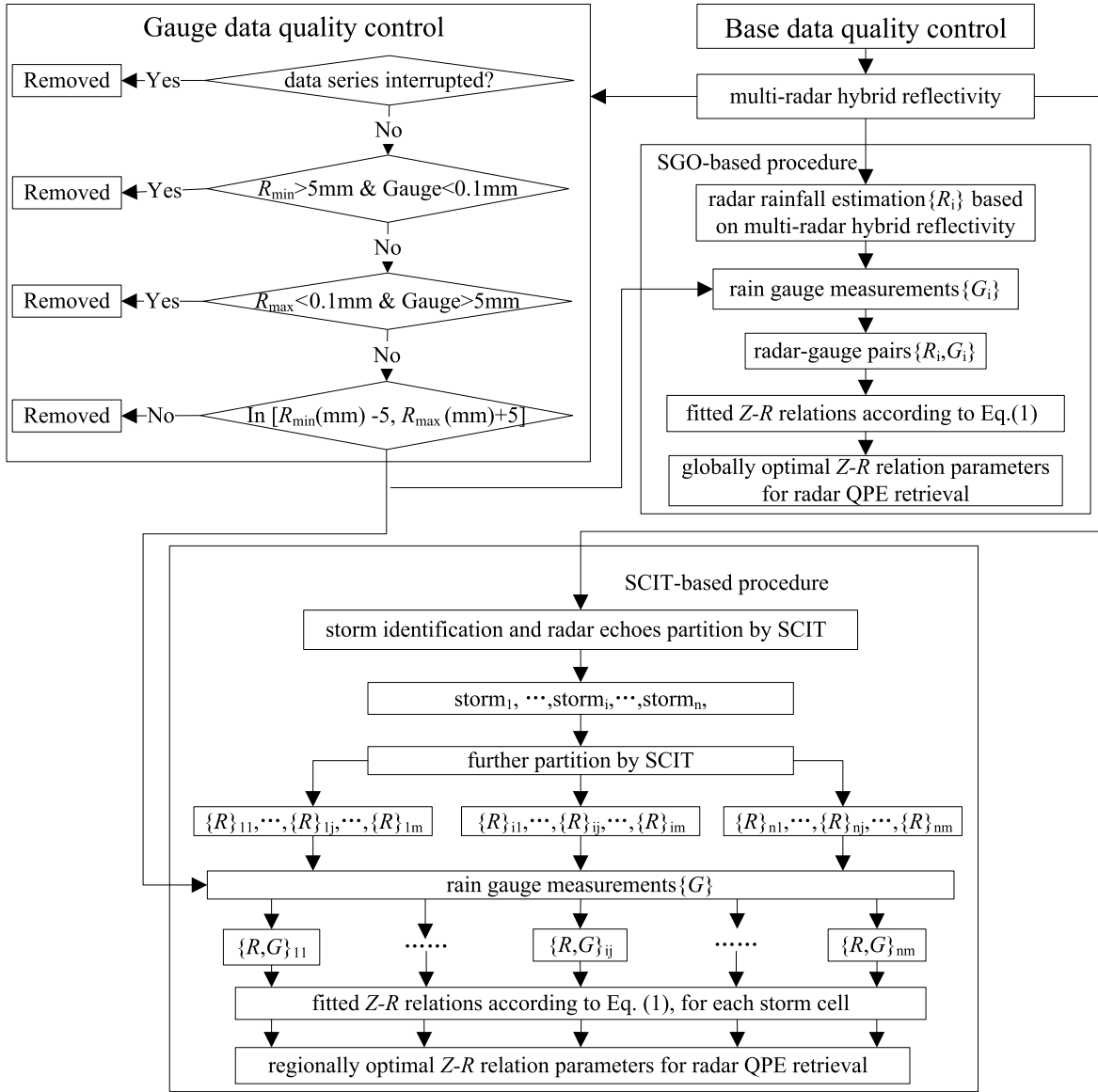


Fig. 1. Flowchart for rain gauge data quality control, and the SGO- and SCIT-based rainfall approaches.

each vertical level of the storm cell can be expressed as

$$\bar{Z}_k(Z_t) = \frac{1}{N(S)} \sum_{(i,j) \in S} Z(i, j, k) \quad (2)$$

where $Z(i, j, k)$ is the reflectivity at Cartesian coordinate (i, j) at the k th level of the multiradar 3-D reflectivity mosaic product; S is the area of storm cell bottom on the MHMR field identified by the SCIT algorithm using reflectivity threshold of Z_t ; $N(S)$ is the number of grid pixels within the area S .

The storm core can be gradually distinguished from its surrounding area by increasing Z_t . The storm cell VPR information across the rainstorm lifespan or during the predefined time windows can be successively obtained and the VPR time series can be assembled as clusters which serve as an important indicator of the temporal variations of the precipitation microphysics. The different characteristics of VPR clusters for different storm cells also highlight the need for dynamic radar

rainfall relations that can represent the changing precipitation microphysics.

III. APPLICATION IN THE EJRB OF CHINA

A. Study Domain

In order to demonstrate the performance of various radar rainfall algorithms, this article selects the EJRB in China as the study domain. Fig. 2 illustrates the digital elevation model (DEM) information of China and the EJRB area in particular. The EJRB area (116°E–123°E, 30.5°N–35.25°N) covers Jiangsu province, Shanghai city, southern part of Shandong province, eastern part of Anhui province and northern part of Zhejiang province, containing the major part of the Yangtze River Delta which is the largest urban region supporting the most prosperous economy in China.

Although there are many small hills, the altitude of most parts of this region is below 50 m above the mean sea level.

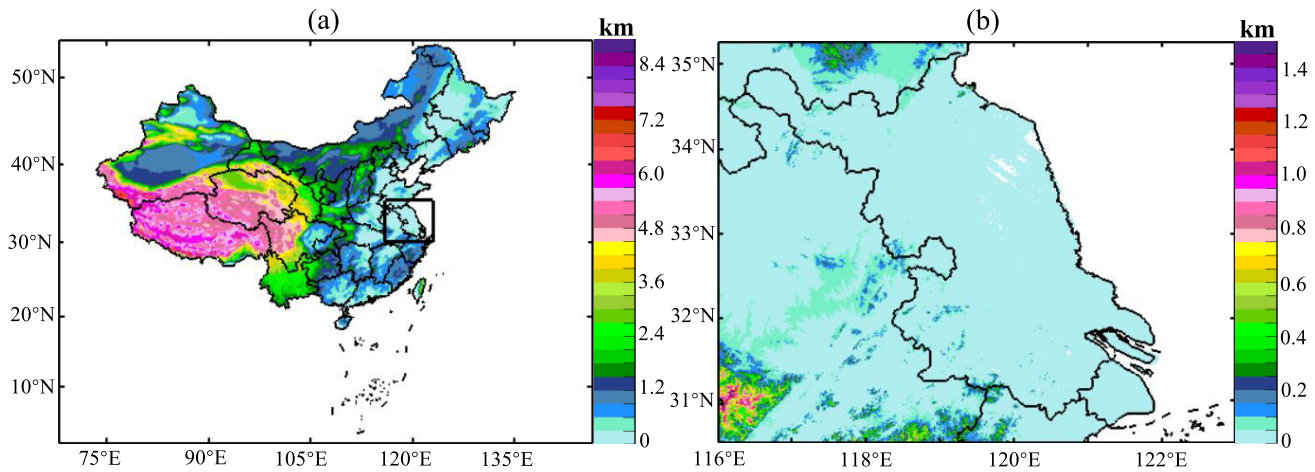


Fig. 2. DEM information of (a) China and (b) EJRB area [indicated by the black rectangle in (a)].

TABLE I
FOUR TYPICAL WEATHER EVENTS OVER THE EJRB AREA

Event #	Timespan	Number of frames	Synoptic remarks
Event 1	0100UTC 09 August - 0000UTC 11 August 2015	471	Super typhoon Soudelor
Event 2	0100UTC 21 June - 0400UTC 22 June 2016	321	Mesoscale convergence line
Event 3	0300UTC 23 June - 1500UTC 23 June 2016	151	Squall line accompanying with hailstorms
Event 4	0100UTC 09 July - 1800UTC 10 July 2017	411	Persistent convective rainfall

This area is primarily featured by the subtropical monsoon (Meiyu monsoon) climate. The synoptic signatures during summer storm seasons in this region are characterized by a warm and wet environment with abundant vapors aggregating in the atmospheric layers below 850 hPa, which provides good moisture conditions for the formation of severe convective rainfall. In addition to bringing abundant water resources to the distributed freshwater lakes and rivers, the disastrous weather events such as extreme precipitation often create substantial negative impacts on regional economics. Therefore, accurate QPE is critical to inform the decision process for water managers that are balancing the competing needs for water supply and flood mitigation.

B. Radar and Gauge Network

Sixteen S-band Doppler weather radars over the EJRB area are used in this article. Fig. 3(a) shows the locations and coverage information of these radars. The height of the MHMR field used for radar QPE applications is also depicted in Fig. 3(a). Most of the regions have low-level coverage (<1 km), indicating the great potential of using this radar network to observe severe weather phenomena close to the surface. All the 16 radars are operational systems deployed for providing severe weather warning and nowcast services for the EJRB region. The radial and azimuthal resolutions are configured as 1000 m and 0.98° , respectively. For routine meteorological operations, the scan strategy for each radar is configured as standard volume coverage pattern (VCP) including 11 scanning elevation angles: 0.5° , 1.5° , 2.4° , 3.5° , 4.9° , 5.6° , 6.5° , 7.9° , 9.5° , 14.5° , and 19.5° . A volume scan in

this VCP mode can be completed in approximately 6 min. The radar base-level data packets are enveloped and streamed to the data processing server every 6 min for further data processing and product generation.

Fig. 3(b) shows the rain gauge locations in the EJRB area. In total, there are 4579 rain gauges operationally deployed in this particular domain. Such a dense rain gauge network can effectively be utilized to capture the overall precipitation pattern and intensities in this region. In this article, 2289 gauge stations are used to derive the dynamic radar rainfall algorithms described in Section II, whereas 2290 stations are used to evaluate various radar rainfall algorithms. Most of these stations are tipping-bucket gauges configured with 1-min temporal resolution in order to provide a fine-scale measurement of rainfall time series, and only time series with no interruption report are used. The SGO- and SCIT-based radar QPE algorithms are evaluated using gauge data at an hourly scale to avoid the measurement errors of rain gauges, especially during light rain [19].

In addition, a simple quality control process (see Fig. 1) is imposed on the gauge data. If the hourly rainfall record from gauge is less than 0.1 mm but the corresponding radar estimate is greater than 5 mm, the gauge data are deemed as false recording and the gauge is suspected to be jammed by tree leaves or insects. Otherwise, if the gauge rainfall record is greater than 5 mm but the radar estimate is less than 0.1 mm, the gauge data are also considered false reading. Furthermore, the potential maximum (R_{\max}) and minimum (R_{\min}) hourly rainfall measurements from gauges are estimated using radar reflectivity aloft based on two empirical $Z-R$ relationships: $Z = 640R^{1.6}$ and $Z = 200R^{1.6}$. The gauges whose hourly

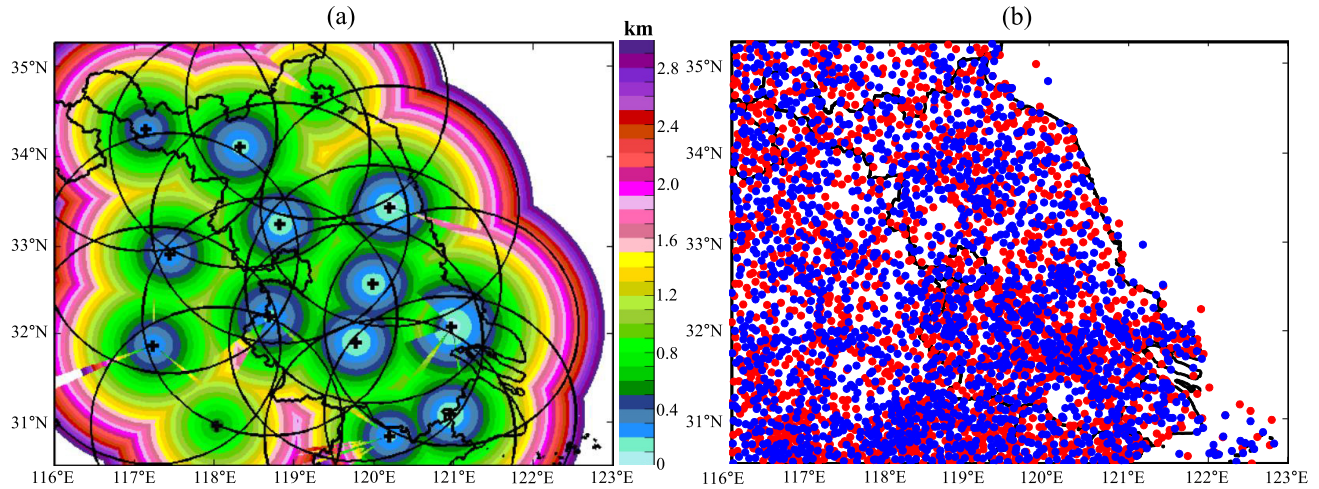


Fig. 3. Radar and gauge network over the EJRB area. (a) 150-km coverage ranges (black circles) of each radar site and height of the MHMR field. (b) Rain gauges are uniformly portioned into training (2289 sites in blue) and testing (2290 sites in red) data sets.

rainfall measurements fall outside of $[R_{\min} - 5, R_{\max} + 5]$ are also eliminated from the raw data.

C. Precipitation Events

Four typical precipitation events over the EJRB area are selected to demonstrate the proposed rainfall estimation system. Table I describes the overall time spans and synoptic signatures of these four events. Fig. 4 shows sample reflectivity observations during these four events. In particular, nine storm cells (indicated by the circles in Fig. 4) are identified from the MHMR fields. Although the reflectivity structures of these nine cells show some similarity, the detailed precipitation characteristics are different from each other. Fig. 5 shows the vertical cross sections of these storm cores, and the location information of the cross section lines is detailed in Table II. Fig. 6 illustrates the VPR clusters of these nine identified cells to resolve the transition of rainfall states during their lifecycles. Table III lists the numbers of VPR profiles associated with each storm cell as well as their starting and ending time. The $Z-R$ relations derived for the individual storm cells are also presented in Table III. The vertical cross sections and VPR clusters of these storm cells are useful to reveal the spatial differences and temporal evolution of the whole rainstorm system.

1) *Event 1*: Event 1 was mainly caused by the peripheral rainfall system of typhoon Soudelor, which was gradually weakening after its landfall in Fujian province of China around 20:40 UTC, August 8, 2015. After Soudelor moved to Anhui province, it receded as a low-pressure circulation at 09:00 UTC, August 10, 2015. Then, this circulation transformed into a temperate cyclone and moved into Jiangsu province, and then to the Yellow Sea near Yancheng City, Jiangsu. During typhoon Soudelor, the maximum gauge 6-h rainfall measurement reached 262 mm at 10:00 UTC, August 10, 2015, which occurred at Chengou village near the entrance of Hongze Lake.

Massive rainstorms were accompanied during typhoon Soudelor. Storm cells 1 and 2 in Fig. 4(a) were identified

TABLE II

CROSS SECTION LINE INFORMATION OF THE STORM CELLS IN FIGS. 4 AND 5. THE STARTING AND ENDING POINTS ARE INDICATED BY (LONGITUDE, LATITUDE)

Subplot in Fig. 4	Cells in Fig. 5	Starting Point	Ending Point
(a)	1 and 2	(118.50°, 30.05°)	(121.0°, 32.75°)
(b)	1	(118.75°, 33.15°)	(120.55°, 32.6°)
(c)	3	(118.50°, 31.75°)	(120.5°, 32.05°)
(d)	3 and 4	(119.875°, 31.45°)	(120.75°, 32.4°)
(e)	5, 6 and 7	(117.55°, 34.95°)	(119.4°, 33.35°)
(f)	5, 6 and 7	(118.25°, 31.75°)	(119.95°, 33.65°)
(g)	8	(118.25°, 34.05°)	(119.5°, 33.85°)
(h)	8 and 9	(119.05°, 32.0°)	(120.5°, 34.85°)

using the reflectivity threshold of 35 and 40 dBZ, respectively, at 05:00 UTC, August 10, 2015. Cell 2 (inner circle) was essentially the storm core area of cell 1 (outer circle), and the cell 2 quickly dissipated with the typhoon gradual weakening. After 4 h, the widespread rainstorm transformed into a stage as shown in Fig. 4(b) and only storm cell 1 was identified at 09:00 UTC, August 10, 2015.

The storm-scale VPR clusters in Fig. 6(a) and (b) both presented obvious tropical rainfall characteristics with radar reflectivity monotonically increasing toward the surface, indicating that higher vapor concentration dominated at the bottom of these two storm cells. In addition, the vertical gradient of the VPR clusters of cell 2 [see Fig. 6(b)] was larger than cell 1 [see Fig. 6(a)], which implies that the rainfall rate in the rainstorm center area was higher than its surrounding areas. During this time period, both of these two storm cells were at the weakening stage, especially cell 2: the reflectivity values of cell 2 were decreasing from the green curve (starting state) to the red curve (ending state), indicating that cell 2 quickly dissipated in this process. Consequently, the spatial structure of the whole rainstorm in Fig. 4(b) and the cross section in Fig. 5(b) show that pixels with reflectivity higher

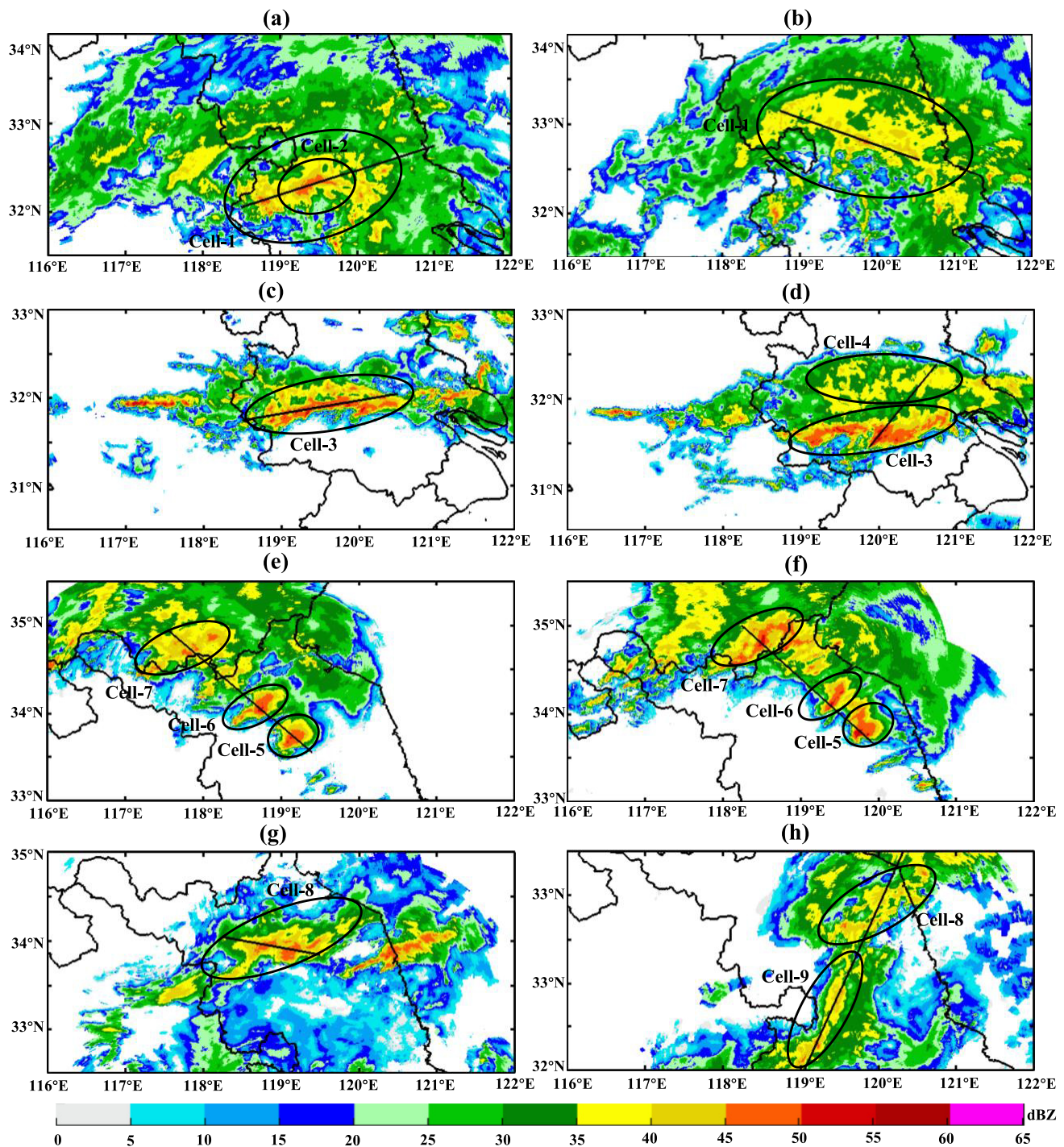


Fig. 4. Storm cell identification results from the MHMR field at (a) 05:00 and (b) 09:00 UTC, August 10, 2015; (c) 22:30 UTC, June 21, 2016, and (d) 00:00 UTC, June 22, 2016; (e) 05:00 and (f) 06:30 UTC, June 23, 2016; (g) 1230 and (h) 19:00 UTC, July 9, 2017. The circles represent the locations of nine identified storm cells and the lines indicate the locations of cross sections illustrated in Fig. 5.

than 45 dBZ were less than that in Fig. 5(a). Although storm cell 1 was apparently enhanced when the green VPR curve transformed into the red curve in Fig. 6(a), such enhancement was essentially caused by the hydrometer diffusion of cell 2.

2) *Event 2*: Event 2 was tightly associated with the interaction of the cold air from the north and warm air from the south, which triggered a nearly horizontal convergence line along the latitude of 32°N. The severe rainfall system featured with typical shapes as depicted in Fig. 4(c) was formed during this process. The maximum 6-h rainfall measurements at Ligang

station reached 148.5 mm at 08:00 UTC, June 22, 2016. Storm cells 3 and 4 are successively identified using the reflectivity threshold of 35 dBZ. With the cold air continuously moving to the south, cell 3 was mainly embedded and sustained in the south part of this rainstorm, whereas cell 4 was detected later at the north side of this rainstorm [see Fig. 4(d)].

Cell 3 was a severe convective rainstorm featured by abundant hydrometers below the altitude of 6 km. The spatial structure illustrated in Fig. 4(c) and (d), and the vertical cross sections in Fig. 5(c) and (d) all showed that most reflectivity

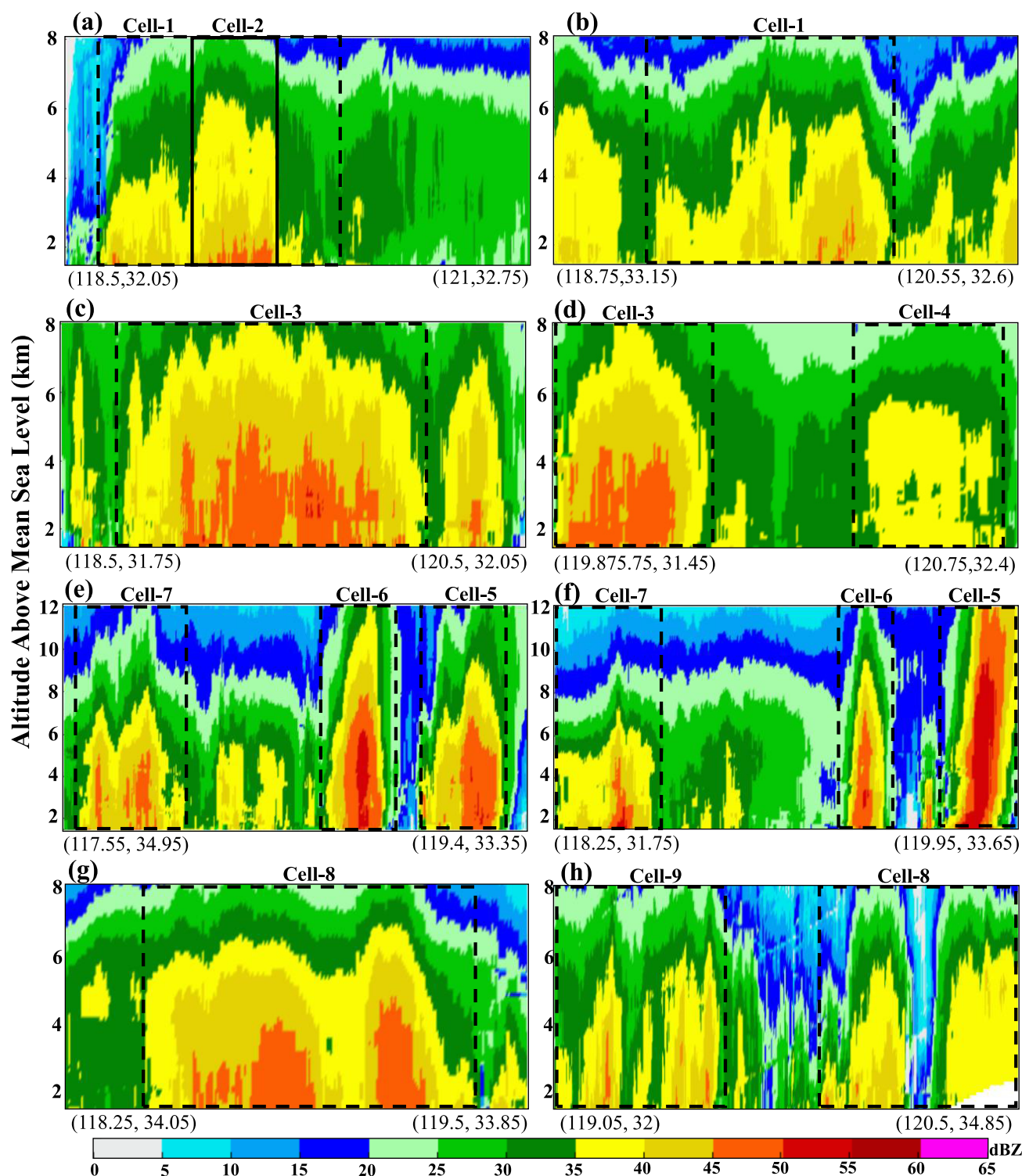


Fig. 5. Cross sections for the eight lines illustrated in Fig. 4. (a) and (b) Cells 1 and 2 in Fig. 4(a) and (b), respectively. (c) and (d) Cells 3 and 4 in Fig. 4(c) and (d), respectively. (e) and (f) Cells 5–7 in Fig. 4(e) and (f), respectively. (g) and (h) Cells 8 and 9 in Fig. 4(g) and (h), respectively. The longitudes and latitudes ($^{\circ}$) of the starting and ending points of these storm cells are marked on the x-axes with their vertical columns marked by the dashed-rectangles.

pixels of cell 3 were larger than 45 dBZ. This also made its VPR cluster [see Fig. 6(c)] featured by a small vertical gradient during its lifespan. In addition, the storm cell 3 had gone through a complex growing and dissipating process, in which its VPR cluster first transformed from the green curve (starting state) at 22:00 UTC, June 21, 2016, to the

blue curve (strongest state) at 23:00 UTC, June 21, 2016, and then gradually weakened into the red curve (ending state) at 00:36 UTC, June 22, 2016, which was similar to the starting state.

The rainfall characteristics of cell 4 were very different from cell 3. Although its reflectivity structure was much

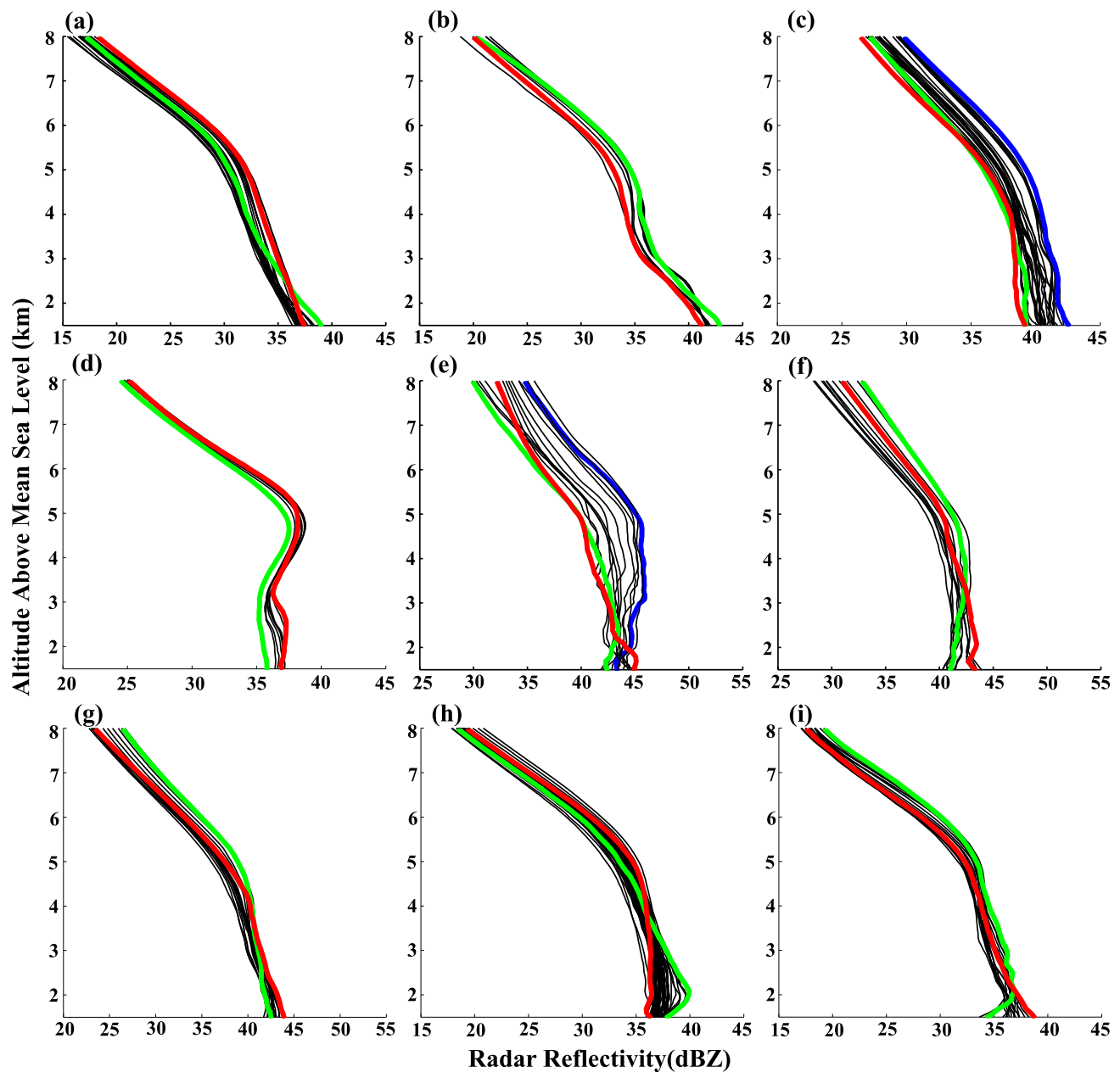


Fig. 6. Storm-scale VPR clusters of the nine storm cells detailed in Table III. The green and red curves represent their starting and ending states. The blue curves in (c) and (e) respectively represent the strongest state of cells 3 and 5. (a) Cell-1. (b) Cell-2. (c) Cell-3. (d) Cell-4. (e) Cell-5. (f) Cell-6. (g) Cell-7. (h) Cell-8. (i) Cell-9.

TABLE III
TIMESPANS OF THE STORM-SCALE VPR CLUSTERS IN FIG. 6 AND CORRESPONDING $Z-R$ RELATIONSHIPS

Cell #	Number of VPR Profiles	Start Time	End Time	(A, b) parameters of $Z = AR^b$
1	25	0500UTC 10 August 2015	0900UTC 10 August 2015	(47.486, 1.860)
2	10	0500UTC 10 August 2015	0554UTC 10 August 2015	(137.368, 1.463)
3	31	2200UTC 21 June 2016	0036UTC 22 June 2016	(16.164, 2.466)
4	18	2330UTC 21 June 2016	0136UTC 22 June 2016	(258.281, 1.396)
5	21	0530UTC 23 June 2016	0730UTC 23 June 2016	(65.515, 1.717)
6	11	0530UTC 23 June 2016	0630UTC 23 June 2016	(91.160, 1.538)
7	11	0530UTC 23 June 2016	0630UTC 23 June 2016	(41.525, 1.927)
8	48	1300UTC 09 July 2017	1854UTC 09 July 2017	(52.284, 1.864)
9	17	1512UTC 09 July 2017	1900UTC 09 July 2016	(33.168, 2.193)

weaker than cell 3, it was featured by the enhanced reflectivity caused by the melting layers near the altitude of 5 km [see Fig. 6(d)]. Nevertheless, the vertical structure of reflectivity was different from the typical VPR curve of stratiform rain in the cold seasons which was monotonically decreasing toward the surface below the melting layer. The warm and wet environments at the bottom of storm cell 4 hindered its VPR from continuously decreasing toward the surface. As a result, warm stratiform rain predominated in cell 4, which was prone to heavier rainfall than the stratiform rain in cold seasons.

3) *Event 3*: Event 3 was initially triggered by the northeast low-level jet stream and the southwest high-level jet stream. Both severe tornado and hails were reported in the Funing town of Yancheng City at 06:30 UTC, June 23, 2016. Then a squall line with severe convective rainstorms moved quickly from the northwest to the southeast over the EJRB area. The maximum 6-h rainfall measurement during this event reached 148.8 mm at Lanling station at 10:00 UTC, June 23, 2016. Severe convective cells 5–7, illustrated in Fig. 4(e) and (f), were successively identified based on the reflectivity threshold of 40 dBZ. In addition, the reflectivity values within the core areas of these cells were higher than 55 dBZ. The VPR clusters of these three storm cells were illustrated in Fig. 6(e)–(g).

Cell 5 was associated with a developing tornado, and short-time hailfall was also reported afterward. The small change of the VPR cluster in Fig. 6(e) demonstrated that the rainfall state below the altitude of 2 km was fairly stable during its lifespan, resulting in that the green curve (starting state) at 05:00 UTC, June 23, 2016, and the red curve (ending state) at 07:30 UTC, June 23, 2016, were nearly overlapped. However, cell 5 exhibited a complex microphysical transition above 2 km. It was quickly enhanced into a mature state (blue curve) at 06:30 UTC, June 23, 2016, which also corresponded to the hailstone developing phase when the small hailstones were evolving to larger hailstones. The spatial structure in Fig. 4(f) showed more obvious “hook” shapes than that in Fig. 4(e). The vertical structure of reflectivity in Fig. 5(f) illustrated that its vertical structure was abnormally enhanced and the core area was featured by more pixels of reflectivity >50 dBZ than that in Fig. 5(e). The echo top extended from 7 to nearly 12 km. Afterward, the VPR gradually transformed into the red curve with a slight reflectivity enhancement from 42.5 to 45 dBZ below 2 km, which coincided with the hail falling process.

Cell 6 was a typical convective thunderstorm and it was strongly developing at the initial state (green curve), which resulted in the severe convective core below the altitude of 7 km in Fig. 5(e). Although it showed a similar spatial structure to cell 5, it was not further enhanced but transformed into a weaker rainstorm. The core area below 7 km in Fig. 5(f) presented much less pixels with reflectivity higher than 45 dBZ. Such a transition made the VPR shapes in Fig. 6(f) characterized by weaker reflectivity as the altitude increases, and the rainfall rate was fairly stable, which gradually dominated the precipitation phase.

Although the spatial structure of cell 7 [see Fig. 4(f)] presented obvious enhancement compared with that in Fig. 4(e), its vertical structure in Fig. 5(e) and (f) were similar to each other, which was also similar to the vertical cross section of

cell 6 in Fig. 5(f). In addition, the VPR cluster of cell 7 in Fig. 6(g) had nearly the same shapes across its lifespan, indicating that there was no obvious transition of the rainfall regime, very similar to that of cell 1 in Fig. 6(a) which was a typical tropical rainstorm, but reflectivity of cell 7 was much stronger. As such, it was concluded that the rainfall of cell 7 was characterized by abundant raindrops similar to a tropical rainfall system, but it was featured by much more severe rainfall than storm cell 1.

4) *Event 4*: Event 4 was a continuous severe rainfall system mainly caused by the interaction of cold air from the north and the warm air from southwest near the north edge of Jiangsu. Heavy rainstorms were triggered near the latitude of 34°N as depicted in Fig. 4(g), and the rainstorms sustained nearly 6 h. After 6.5 h, there was still a large area of rainstorm in Fig. 4(h) near the latitude of 34°N . During this event, there were many rain gauge stations that recorded 6-h rainfall exceeding 100 mm and the maximum 6-h rainfall reached 232.6 mm at Liren country at 18:00 UTC, July 9, 2017. Both storm cells 8 and 9 were identified using the reflectivity threshold of 35 dBZ.

Cell 8 was initially triggered at 08:00 UTC, July 9, 2017, and it was present in both Fig. 4(g) and (h), indicating its long lifespan. Its VPR curve at the starting stage was featured with the reflectivity bump below 4 km [see Fig. 6(h)], which implied that cell 8 was in an unstable convective developing state in the initial phase. Afterward, cell 8 transformed into a stable convective rainfall state (black and red curves) and the reflectivity on all the layers below 5 km were nearly the same, which can also be clearly seen in Fig. 5(g). Its vertical structure shifted very little in Fig. 6(h) and was fairly consistent for nearly 6 h until cells 8 and 9 merged into one huge rainstorm at 19:00 UTC, July 9, 2017.

Cell 9 was formed and identified latter at 15:12 UTC, July 9, 2017. Its initial VPR curve in Fig. 6(i) presented a similar shape to the initial state of cell 8 in Fig. 6(h). However, it quickly transformed into a convective rainstorm. Although the vertical reflectivity in Fig. 5(h) was weaker than cell 8, the reflectivity structure of cell 9 was also characterized by a decreasing trend as the altitude increased, which was similar to that of cells 1, 2, and 7.

As shown previously, each identified storm cell during the four precipitation events had its unique heterogeneous rainfall characteristics, and the differences between some storm cells could be dramatic. This, again, highlights the requirement of more representative Z – R relationships that can capture the local rainfall characteristics for improved QPE.

IV. RESULTS AND DISCUSSION

As mentioned, the gauge stations over the EJRB area are uniformly separated into two groups: the training data set and the test data set [see Fig. 3(b)]. The training data set is used to derived dynamic Z – R relationships, and the testing data are used for evaluation of the radar-derived hourly rainfall estimates.

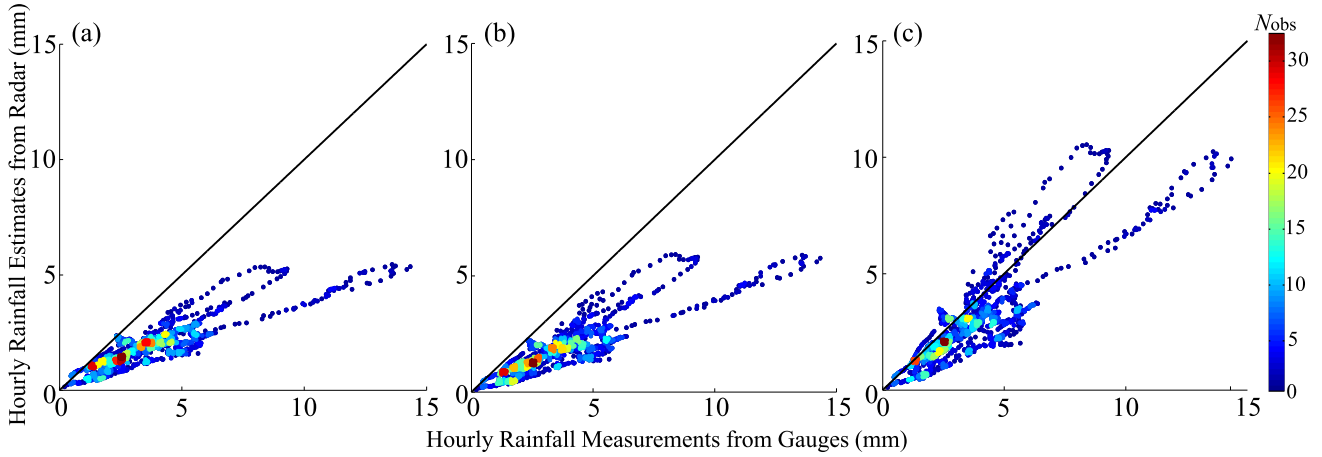


Fig. 7. Scattergram of hourly rainfall estimates from radar versus gauges. (a)–(c) are respectively derived from stratiform, convective, and tropical rainfall relations. (a) $Z = 200R^{1.6}$. (b) $Z = 300R^{1.4}$. (c) $Z = 253R^{1.25}$.

A. Evaluation Metrics

Three evaluation metrics are computed at the validation gauge locations for quantitative assessment, including the normalized mean error (E_{NMB}), root-mean-square error (E_{rms}), and the Pearson correlation coefficient (E_{CC})

$$E_{\text{NMB}} = \frac{\sum_{i=1}^n (r_i - g_i)}{\sum_{i=1}^n g_i} \quad (3a)$$

$$E_{\text{rms}} = \sqrt{\frac{1}{n} \sum_{i=1}^n |r_i - g_i|^2} \quad (3b)$$

$$E_{\text{CC}} = \frac{\sum_{i=1}^n (g_i - \bar{g})(r_i - \bar{r})}{\sqrt{\sum_{i=1}^n (g_i - \bar{g})^2 \sum_{i=1}^n (r_i - \bar{r})^2}} \quad (3c)$$

where g and r denote the hourly rainfall measurements from gauge and corresponding radar observations, respectively; the overbar $\bar{\cdot}$ stands for the sample average. E_{NMB} reflects the overall bias of the radar estimated rainfall. E_{rms} is an important indicator of the local error of radar-derived rainfall, whereas E_{CC} reflects the correlation between the radar estimates and gauge measurements.

Positive (negative) E_{NMB} scores represent the overestimation (underestimation) of radar rainfall estimates. Smaller E_{rms} indicates smaller error of the radar estimated rainfall, and larger E_{CC} means radar estimates are more consistent with corresponding rain gauge measurements.

The evaluation scores are calculated at the same temporal resolution as the update rate (i.e., 6 min) of radar hourly QPE product. In addition, the radar-gauge pairs are excluded in the calculation if g_i is less than 0.1 mm or the total number of valid validation gauges is less than 10. Such a constraint aims to further improve the confidence of the evaluation results.

B. Results

There are 1354 time frames for all the four precipitation events detailed in Section III-C, which include 1 558 480 radar-gauge hourly rainfall pairs. Radar estimates are derived using various rainfall algorithms, and the performance is cross-compared.

1) Comparison Between Individual Z–R Relations: The radar rainfall relations $Z = 300R^{1.4}$, $Z = 200R^{1.6}$, and $Z = 230R^{1.25}$, respectively representing convective, stratiform, and tropical rainfall, are applied first for the four precipitation events. Fig. 7 shows the scatter plots of radar rainfall estimates using these three Z–R relations versus gauge observations. It can be seen from Fig. 7(a) and (b) that the traditional convective and stratiform rainfall relationships have similar scatter distributions and both are showing substantial underestimation. In addition, as detailed in Table IV, their E_{rms} and E_{CC} scores are close and E_{NMB} scores are negative for all the four events. Although the tropical rainfall relation results in some scatters above the 1:1 line in Fig. 7(c) (i.e., overestimation), the majority of the scatters are distributed below the 1:1 line, indicating an overall underestimation. Scrutinizing the evaluation results in Table IV, the underestimation of the tropical rainfall relation is found for events 1, 3 and 4, while it is overestimating rainfall during event 2. Nevertheless, the tropical rainfall relation has superior performance to both the convective and stratiform relations in terms of E_{NMB} , E_{rms} , and E_{CC} . As shown in Fig. 7(c), the radar rainfall estimates agree fairly well with gauge observations especially in [0 mm, 5 mm].

The comparison between these three conventional Z–R relations implies that the precipitation events are close to tropical rainfall, although only event 1 is directly related to typhoon. Such rainfall characteristics are tightly associated with abundant hydrometeors at the low atmospheric layers during the summer monsoon seasons in China. In addition, the coexistence of overestimation and underestimation of the tropical rainfall algorithm emphasizes the possible differences in rain regimes, which requires adaptive Z–R relationships to capture such differences.

2) Comparison Between Dynamic Z–R Relations: The SGO-based approach temporally adjusts the radar rainfall relations, although a single Z–R relation is applied for the whole domain at a certain time. As a result, the SGO-based rainfall estimates have better performance than those derived from the fixed rainfall relations, in terms of E_{NMB} , E_{rms} , and

TABLE IV
PERFORMANCE SCORES OF HOURLY RAINFALL ESTIMATES FROM RADAR USING THREE SINGLE $Z-R$ RELATIONSHIPS

Event #	Total Frames	$Z = 200R^{1.6}$			$Z = 300R^{1.4}$			$Z = 230R^{1.25}$		
		E_{NMB} (%)	E_{RMS} (mm)	E_{CC}	E_{NMB} (%)	E_{RMS} (mm)	E_{CC}	E_{NMB} (%)	E_{RMS} (mm)	E_{CC}
Event 1	471	-42.19	4.63	0.73	-47.48	4.33	0.75	-22.78	3.58	0.79
Event 2	321	-42.38	4.85	0.74	-41.5	4.56	0.77	17.09	4.08	0.79
Event 3	151	-59.07	10.48	0.71	-56.72	9.93	0.74	-41.63	8.76	0.78
Event 4	411	-48.98	4.17	0.72	-52.58	4.1	0.76	-28.46	3.15	0.79

TABLE V
PERFORMANCE SCORES OF RADAR RAINFALL ESTIMATES USING THE SGO- AND SCIT-BASED APPROACHES

Event #	Total Frames	SGO-based Algorithm			SCIT-based Algorithm		
		E_{NMB} (%)	E_{RMS} (mm)	E_{CC}	E_{NMB} (%)	E_{RMS} (mm)	E_{CC}
Event 1	471	-3.38	3.14	0.80	0.99	2.34	0.90
Event 2	321	16.38	3.81	0.84	-0.01	2.46	0.94
Event 3	151	-11.9	7.41	0.82	-6.9	4.96	0.93
Event 4	411	21.97	5.69	0.79	3.35	1.92	0.92

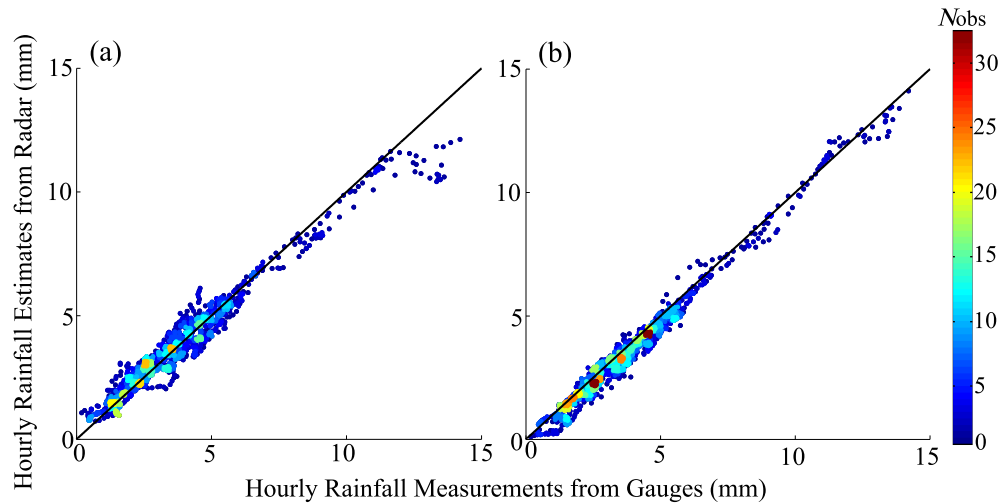


Fig. 8. Scattergram of the spatially averaged hourly rainfall estimates from radar versus gauges: (a) and (b) are respectively derived from the SGO- and SCIT-based algorithms. The spatial average refers to the mean of radar and gauge rainfall estimates at all the validation gauge locations at a certain time frame. The number of scatters is the same as the number of time frames.

E_{CC} (see Table V). It is also noted that the E_{NMB} scores of the SGO-based algorithm in Table V are negative except for event 2, indicating underestimation during most of the events. However, compared to the scatter plots in Fig. 7, the underestimation [see Fig. 8(a)] is not significant.

In order to quantify the QPE uncertainties induced by the nonuniform distribution of precipitation, Fig. 9 illustrates the scatter plots of hourly rainfall estimates from radar versus gauges at all the validation gauge locations and for all the 1558480 pairs during these four validation events. Fig. 9(a) shows that the hourly rainfall product derived using the SGO-based algorithm is inclined to underestimate the rainfall, which also accounts for the underestimation of spatially-averaged hourly rainfall estimates in Fig. 8(a) and the negative E_{NMB} scores in Table V. In addition, we have checked nine radar grid pixels in the vicinity of each gauge station. If the grid pixel with the minimum difference between radar and gauge

is selected for comparison, the evaluation scores will be further improved [see Fig. 9(b)]. Nevertheless, noticeable differences between radar estimates and gauge observations still exist, likely due to the nonuniform distribution of rainfall as shown in the detailed microphysical analysis in Section III.

As mentioned previously, the SCIT-based dynamic rainfall approach partitions the radar reflectivity and gauge stations into many smaller groups to obtain more geophysically characterized $Z-R$ relationships for different storm regions. It automatically differentiates the rainfall regimes through the parameterization of $Z-R$ relations. Fig. 8(b) shows the scattergram of the spatially averaged hourly rainfall derived from the SCIT-based approach at each time frame. Obviously, the scatters are more concentrated compared to Fig. 8(a). Fig. 10 illustrates the detailed comparison of the evaluation scores of the SCIT- and SGO-based rainfall algorithms for all the time frames during these four precipitation events.

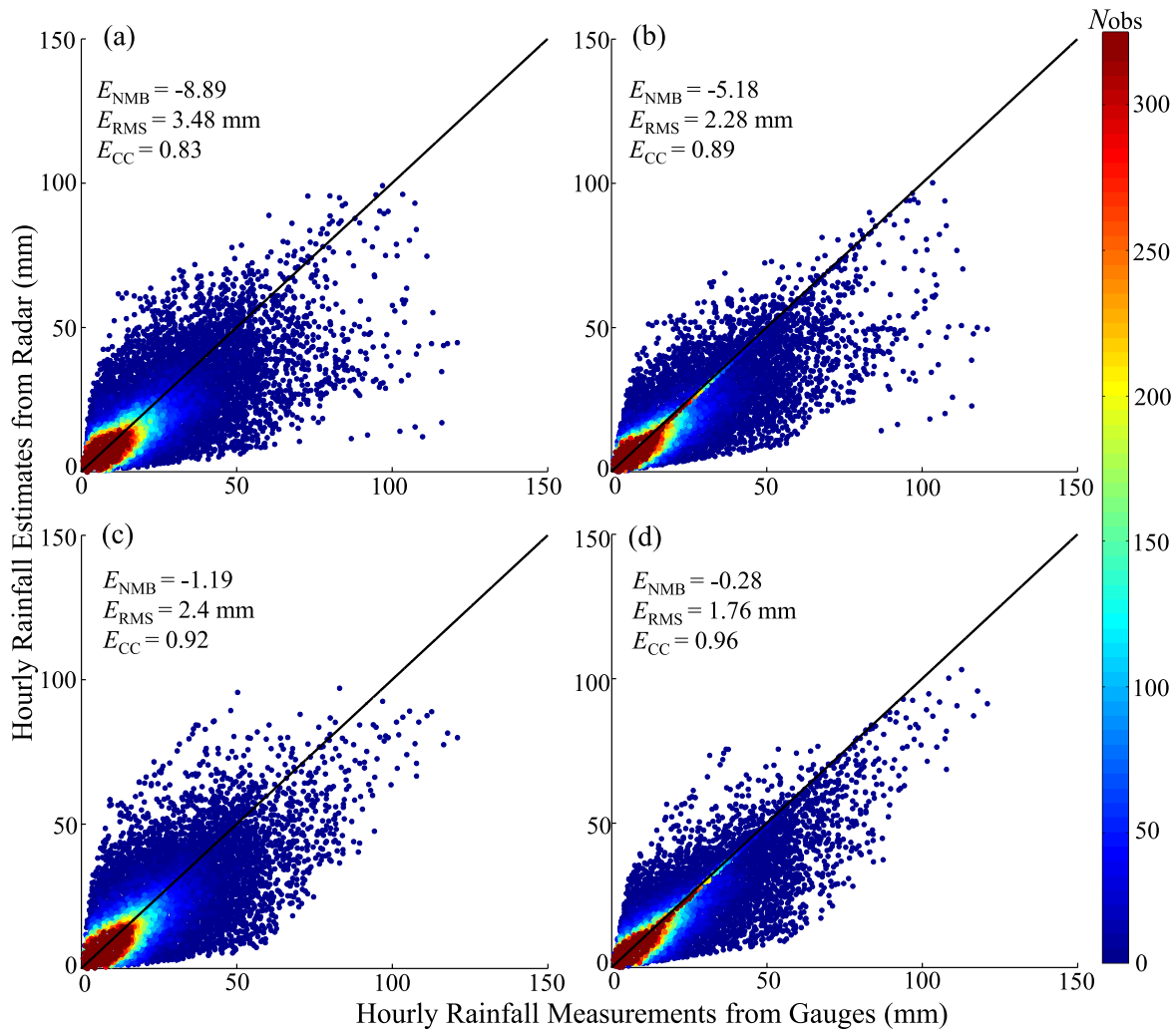


Fig. 9. Scattergram of hourly rainfall estimates from radars versus gauges at all validation gauge stations. (a) is derived from the SGO-based algorithm; (b) is the same with (a), but a nearby radar grid pixel closer to the gauge measurement is selected for comparison; (c) and (d) are the same with (a) and (b), but for the SCIT-based algorithm.

It is concluded that the SCIT-derived radar rainfall estimates outperform the SGO-based estimates during most of the time frames. Although substantial improvement has been achieved, the SCIT-based radar rainfall estimates still show some underestimation [see Fig. 8(b)], which is similar to the underestimation of the SGO-based results indicated in Fig. 8(a) when the spatially averaged hourly rainfall intensity is high.

In addition, the SCIT-based results in Fig. 9(c) show improved performance than Fig. 9(a), with more scatters distributed along the 1:1 line. We also want to note that if the grid pixel (from nine surrounding pixels) with the minimum difference between radar and gauge is selected for evaluating the SCIT-based algorithm, the best performance scores can be achieved [see Fig. 9(d)]. This indicates that some validation gauges may be close to the edge of the identified storm cells which could possibly result from the wind effect.

In summary, the performance of radar hourly rainfall estimates in Fig. 9(c) and (d) is incrementally improved, and Fig. 9(c) and (d), respectively show better performance than Fig. 9(a) and (b). The superior performance of the SCIT-based approach to the SGO-based algorithm can be attributed to the effective reflectivity partitioning, i.e., the more representative

$Z-R$ relationships are adopted, the more reasonable rainfall field can be derived. In order to further demonstrate partitioning impact, the $Z-R$ relation for each of the nine identified cells in Section III is fit and illustrated in Fig. 11. It should be noted that the rainfall rates used for fitting are derived from gauges within the coverage of each storm cell. The specific (A , b) parameters are listed in Table III, which quantitatively shows the parameterization differences of different rainfall regimes. These optimal $Z-R$ relationships are directly associated with the storm-scale VPR clusters in Fig. 6 and represent the rainfall features better than any single $Z-R$ relation.

C. Discussion

Although the SCIT-based dynamic radar rainfall algorithm can substantially improve the radar QPE performance, extra attention should be paid to a number of issues when using a single-polarization radar. All these issues may affect the fitting of $Z-R$ relations with current radar and gauge measurements.

- 1) *The Attenuation Issue:* Although the radar systems used in this article are S-band, which is less affected by attenuation especially during light to moderate rain

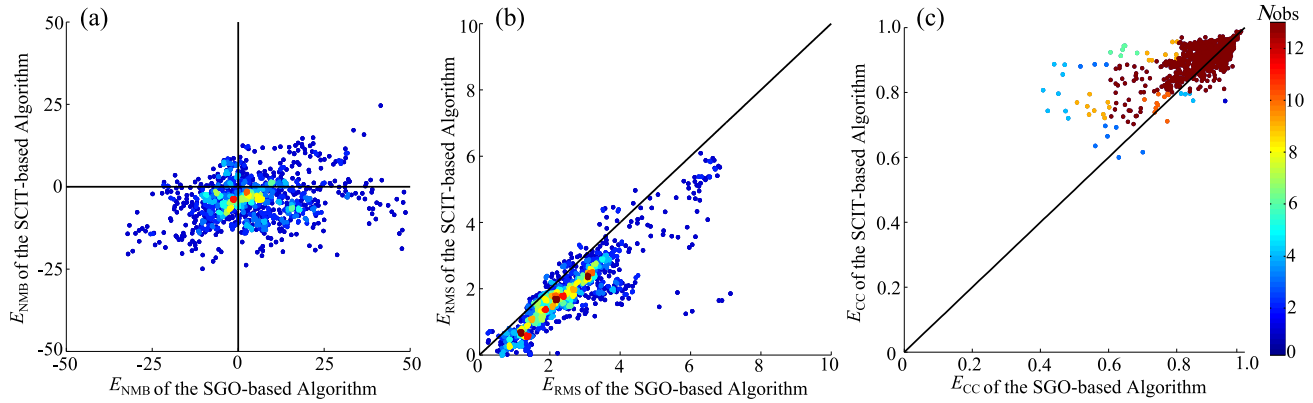


Fig. 10. Comparison of the evaluation scores of the SCIT- and SGO-based rainfall algorithms. (a) $E_{NMB}(\%)$. (b) $E_{RMS}(mm)$. (c) E_{CC} .

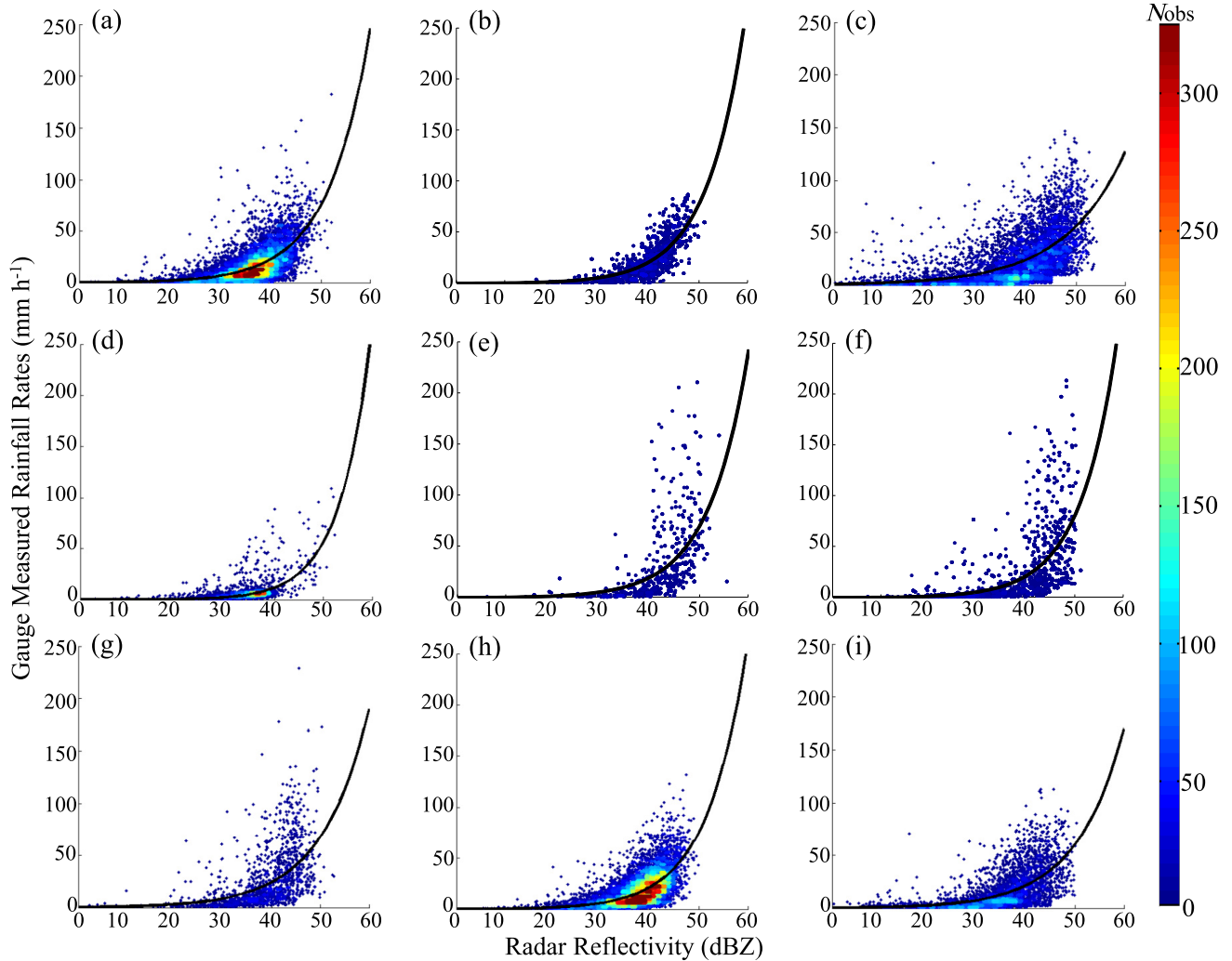


Fig. 11. Gauge-derived rainfall rates versus radar reflectivity within the coverage of nine rainstorms listed in Table III. (a) Cell-1. (b) Cell-2. (c) Cell-3. (d) Cell-4. (e) Cell-5. (f) Cell-6. (g) Cell-7. (h) Cell-8. (i) Cell-9. (a)–(i) are respectively related to Cells 1–9 and the black curves represent the fit power-law relations.

scenarios. For example, Fig. 11(b) and (d) shows the respective scatter plots for the tropical rainstorm core (cell 2) and a stratiform rain region (cell 4). Both $Z-R$ fitting curves exhibit exponential characteristics, which is consistent with typical $Z-R$ model. However, the scattergrams in Fig. 11(e)–(g), which are respectively for the storm cells 5–7, show substantial fluctuations in the

high reflectivity range [40 dBZ, 60 dBZ]. These storm cells essentially represent the severe rainfall regions and ideally more scatters should be along the exponential fitting curves in Fig. 11(e)–(g). But the radar measured reflectivity values in [40 dBZ, 60 dBZ] are lower than expected. Such fluctuations are likely due to the attenuation caused by heavy rain. Unfortunately,

it is challenging to get rid of the attenuation effect for single-polarization radar applications. Polarimetric radar techniques are suggested to address this issue [20]–[23].

- 2) *Mismatch Between Radar Reflectivity and Surface Rainfall*: The radar observes hydrometeors in the atmosphere while rain gauges measure rainfall near the surface. As shown in Fig. 6, the VPR structures of storm cells 1–3, 7, and 9 are more inclined to tropical rain and show a monotonic decreasing trend as the altitude increases. As such, larger reflectivity would be expected near the surface than the measured reflectivity in the MHMR field. In addition, storm cell 2 is very different from the classical stratiform rain during the spring and fall seasons over the EJHB area. Different and possibly more sophisticated VPR correction methods (see [24]–[27]) should be implemented for these types of rainfall.
- 3) *The Uncertainty of Gauge Observations*: The tipping-bucket gauges are often affected by the surface wind and other environmental factors [19], [28]. The falling raindrops may splash out of the bucket, causing underestimation of rainfall in the bucket. In addition, during severe rainfall events, the tipping-bucket may not react as quickly to the sharp rainfall within 1 min, causing undercount of rainfall tips. These observational errors are hard to detect and correct, which can degrade the Z – R relationships in the fitting process. Nevertheless, the tipping-bucket gauge is still the mainstream facility deployed at the national weather monitoring stations in China. With more and more disdrometers are deployed for operational applications, the high-quality information about the local raindrop distribution should be incorporated in the future to derive more robust Z – R relationships.

The first two issues may lead to an underestimation of reflectivity in the MRHR field compared to the intrinsic reflectivity which should be measured near the surface. This is also why the scatter distribution in Fig. 11 is sparse near the reflectivity range of [40 dBZ, 60 dBZ], when the rainfall rates are higher than 75 mm/h. The third issue emphasizes the importance of the high-quality ground truth since it is the basis of the dynamic radar rainfall approach.

V. CONCLUSION

In this article, two dynamic radar rainfall estimation algorithms are described and demonstrated using radar and gauge measurements over the EJRB area in China. One is based on the single globally optimal (SGO) Z – R relation, and the other is based on a SCIT algorithm. The storm cell scale VPR clusters derived based on the multiradar 3-D reflectivity mosaic grids are investigated to resolve the precipitation characteristics of four typical weather events. The primary conclusions of the storm-scale rainfall microphysical analysis and the QPE evaluation are summarized as follows.

- 1) The storm-scale VPR clusters of the identified storm cells reveal that multiple rainfall regimes coexist during these four precipitation events, which are characterized by different geophysical properties.
- 2) The fixed Z – R relationships statistically fit during the life-cycle of each rainstorm, along with the storm-scale VPR clusters, demonstrate the differences in the parameterization of different rainstorms. Both the SGO- and SCIT-based algorithms show better performance than the fixed Z – R relations, which highlights the need for more adaptive Z – R relationships.
- 3) The rainfall regimes over the EJRB area are more inclined to tropical rainfall. Although the SGO- and SCIT-based rainfall estimators both adapt the Z – R relationships in a dynamic manner, the latter performs much better at most of the time frames. Such superior performance is attributed to the better representative capability of the SCIT-based rainfall approach in different regimes since the Z – R relations are updated frequently in both spatial and temporal domains.

Although it is suggested to apply these dynamic rainfall approaches in regions with ample gauge observations, the approaches should also work in regions with sparse gauge coverage as long as at least one gauge station is available in each identified storm cell. Future work will focus on quantifying the algorithm performance in such regions. In addition, polarimetric observables should be incorporated for dual-polarization radar rainfall applications.

ACKNOWLEDGMENT

The radar and gauge data were provided by the China Meteorological Administration.

REFERENCES

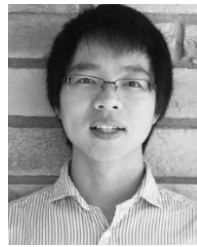
- [1] J. W. Wilson and E. A. Brandes, "Radar measurement of rainfall—a summary," *Bull. Amer. Meteorological Soc.*, vol. 60, no. 9, pp. 1048–1060, 1979.
- [2] H. Chen and V. Chandrasekar, "The quantitative precipitation estimation system for Dallas—Fort Worth (DFW) urban remote sensing network," *J. Hydrol.*, vol. 531, pp. 259–271, Dec. 2015.
- [3] V. N. Bringi and V. Chandrasekar, *Polarimetric Doppler Weather Radar: Principles and Applications*. Cambridge, U.K.: Cambridge Univ. Press, 2001.
- [4] R. A. Fulton, J. P. Breidenbach, D.-J. Seo, D. A. Miller, and T. O'Bannon, "The WSR-88D rainfall algorithm," *Weather Forecasting*, vol. 13, no. 2, pp. 377–395, Jun. 1998.
- [5] J. Zhang *et al.*, "National mosaic and multi-sensor QPE (NMQ) system: Description, results, and future plans," *Bull. Amer. Meteorol. Soc.*, vol. 92, no. 10, pp. 1321–1338, Oct. 2011.
- [6] B. E. Martner, S. E. Yuter, A. B. White, S. Y. Matrosov, D. E. Kingsmill, and F. M. Ralph, "Raindrop size distributions and rain characteristics in California coastal rainfall for periods with and without a radar bright band," *J. Hydrometeorol.*, vol. 9, no. 3, pp. 408–425, Jun. 2008.
- [7] M. Steiner and J. A. Smith, "Reflectivity, rain rate, and kinetic energy flux relationships based on raindrop spectra," *J. Appl. Meteorol.*, vol. 39, no. 11, pp. 1923–1940, Nov. 2000.
- [8] D. Willie *et al.*, "Evaluation of multisensor quantitative precipitation estimation in russian river basin," *J. Hydrologic Eng.*, vol. 22, no. 5, May 2017, Art. no. E5016002.
- [9] R. Cifelli, V. Chandrasekar, H. Chen, and L. E. Johnson, "High resolution radar quantitative precipitation estimation in the san francisco bay area: Rainfall monitoring for the urban environment," *J. Meteorol. Soc. Japan. II*, vol. 96A, pp. 141–155, 2018.
- [10] G. J. Ciach and W. F. Krajewski, "Radar–rain gauge comparisons under observational uncertainties," *J. Appl. Meteorol.*, vol. 38, no. 10, pp. 1519–1525, Oct. 1999.
- [11] D. Legates, "Real-time calibration of radar precipitation estimates," *Prof. Geographer*, vol. 52, no. 2, pp. 235–246, May 2000.

- [12] H. Chen, V. Chandrasekar, H. Tan, and R. Cifelli, "Rainfall estimation from ground radar and TRMM precipitation radar using hybrid deep neural networks," *Geophys. Res. Lett.*, vol. 46, nos. 17–18, pp. 10669–10678, Sep. 2019.
- [13] L. Alfieri, P. Claps, and F. Laio, "Time-dependent Z-R relationships for estimating rainfall fields from radar measurements," *Natural Hazards Earth Syst. Sci.*, vol. 10, no. 1, pp. 149–158, 2010.
- [14] Y. Gou, L. Liu, D. Wang, L. Zhong, and C. Chen, "Evaluation and analysis of the Z-R storm-grouping relationships fitting scheme based on storm identification," (in Chinese), *Torrential Rain Disasters*, vol. 34, no. 1, pp. 1–8, 2015.
- [15] Y. Gou, Y. Ma, H. Chen, and Y. Wen, "Radar-derived quantitative precipitation estimation in complex Terrain over the eastern Tibetan Plateau," *Atmos. Res.*, vol. 203, pp. 286–297, May 2018.
- [16] J. T. Johnson *et al.*, "The storm cell identification and tracking algorithm: An enhanced WSR-88D algorithm," *Weather Forecasting*, vol. 13, no. 2, pp. 263–276, Jun. 1998.
- [17] M. Berenguer, D. Sempere-Torres, C. Corral, and R. Sánchez-Diezma, "A fuzzy logic technique for identifying nonprecipitating echoes in radar scans," *J. Atmos. Ocean. Technol.*, vol. 23, no. 9, pp. 1157–1180, Sep. 2006.
- [18] J. Bech, B. Codina, J. Lorente, and D. Bebbington, "The sensitivity of single polarization weather radar beam blockage correction to variability in the vertical refractivity gradient," *J. Atmos. Ocean. Technol.*, vol. 20, no. 6, pp. 845–855, Jun. 2003.
- [19] H. Chen and V. Chandrasekar, "Estimation of light rainfall using ku-band dual-polarization radar," *IEEE Trans. Geosci. Remote Sens.*, vol. 53, no. 9, pp. 5197–5208, Sep. 2015.
- [20] S. Y. Matrosov, K. A. Clark, B. E. Martner, and A. Tokay, "X-band polarimetric radar measurements of rainfall," *J. Appl. Meteorol.*, vol. 41, no. 9, pp. 941–952, Sep. 2002.
- [21] H. Chen, V. Chandrasekar, and R. Bechini, "An improved dual-polarization radar rainfall algorithm (DROPS2.0): Application in NASA IFloodS field campaign," *J. Hydrometeorol.*, vol. 18, no. 4, pp. 917–937, Apr. 2017.
- [22] A. Ryzhkov, M. Diederich, P. Zhang, and C. Simmer, "Potential utilization of specific attenuation for rainfall estimation, mitigation of partial beam blockage, and radar networking," *J. Atmos. Ocean. Technol.*, vol. 31, no. 3, pp. 599–619, Mar. 2014.
- [23] Y. Gou, H. Chen, and J. Zheng, "An improved self-consistent approach to attenuation correction for C-band polarimetric radar measurements and its impact on quantitative precipitation estimation," *Atmos. Res.*, vol. 226, pp. 32–48, Sep. 2019.
- [24] M. Kitchen, R. Brown, and A. G. Davies, "Real-time correction of weather radar data for the effects of bright band, range and orographic growth in widespread precipitation," *Quart. J. Roy. Meteorological Soc.*, vol. 120, no. 519, pp. 1231–1254, Jul. 1994.
- [25] H. Andrieu and J. D. Creutin, "Identification of vertical profiles of radar reflectivity for hydrological applications using an inverse method. Part I: Formulation," *J. Appl. Meteorol.*, vol. 34, no. 1, pp. 225–239, Jan. 1995.
- [26] A. Bellon, G. W. Lee, and I. Zawadzki, "Error statistics of VPR corrections in stratiform precipitation," *J. Appl. Meteorol.*, vol. 44, no. 7, pp. 998–1015, Jul. 2005.
- [27] H. Chen, R. Cifelli, and A. White, "Improving operational radar rainfall estimates using profiler observations over complex Terrain in Northern California," *IEEE Trans. Geosci. Remote Sens.*, vol. 58, no. 3, pp. 1821–1832, Mar. 2020.
- [28] E. Habib, W. F. Krajewski, and A. Kruger, "Sampling errors of tipping-bucket rain gauge measurements," *J. Hydrol. Eng.*, vol. 6, no. 2, pp. 159–166, Apr. 2001.



Yabin Gou received the B.S. degree in technology of computer application from Nanjing Agricultural University, Nanjing, China, in 2009, and the Ph.D. degree in meteorology from the University of Chinese Academy of Sciences, Beijing, China, in 2014.

He is currently a Senior Engineer with the Hangzhou Meteorological Bureau, Zhejiang, China, where he is also in charge of a C-band operational polarimetric radar. His research interests include radar data quality control, precipitation microphysics, precipitation estimation and nowcasting, and comprehensive analysis of mesoscale and small-scale extreme weather events using radar measurements.



Haonan Chen (Member, IEEE) received the bachelor's degree from the Chongqing University of Posts and Telecommunications, Chongqing, China, in 2010, and the M.S. and Ph.D. degrees from Colorado State University (CSU), Fort Collins, CO, USA, in 2013 and 2017, respectively, all in electrical engineering.

He has been working with the Earth System Research Laboratory, Physical Sciences Division, NOAA, Boulder, CO, USA, since 2012, first as a Research Student, then as a National Research Council (NRC) Research Associate, and currently as a Radar, Satellite, and Precipitation Scientist through the Cooperative Institute for Research in the Atmosphere (CIRA). He is also an Affiliate Faculty Member with the Department of Electrical and Computer Engineering, CSU. His research interest includes mainly to advance the understanding of the physical sciences in the hydrometeorological processes through remote sensing technologies. He also specializes in radar systems and networking, precipitation classification and estimation with polarimetric radar measurements, and multiscale radar and satellite data fusion.

Dr. Chen serves as an Associate Editor for *Journal of Atmospheric and Oceanic Technology* and *URSI Radio Science Bulletin* and as a Guest Editor for *Remote Sensing*.



V. Chandrasekar (Fellow, IEEE) received the bachelor's degree from IIT Kharagpur, Kharagpur, India, in 1981, and the Ph.D. degree from Colorado State University (CSU), Fort Collins, CO, USA, in 1986.

He has played a key role in developing the CSU-CHILL National Radar Facility as one of the most advanced meteorological radar systems available for research and continues to work actively with the CSU-CHILL radar, supporting its research and education mission. He has also been the Director of the Research Experiences for Undergraduate Program, for over 25 years, promoting research in the undergraduate curriculum. He serves as the Research Director of the National Science Foundation Engineering Research Center for Collaborative Adaptive Sensing of the Atmosphere. He is also an Avid Experimentalist conducting special experiments to collect *in situ* observations to verify the new techniques and technologies. He also serves as an Associate Dean of the College of Engineering for promoting International Research Collaboration. He is currently a University Distinguished Professor with CSU. He has been actively involved with research and development of weather radar systems for over 35 years. He has served as an Academic Advisor for over 70 graduate students. He has been a Visiting Professor at the National Research Council of Italy, Rome, Italy; University of Helsinki, Helsinki, Finland; Finnish Meteorological Institute, Helsinki; Tsinghua University, Beijing, China; and IIT Kharagpur, Kharagpur, India. He is an Affiliate Scientist with the NASA Jet Propulsion Laboratory, Pasadena, CA, USA; a Distinguished Visiting Scientist with the NASA Goddard Space Flight Center, Greenbelt, MD, USA; and a Distinguished Professor of Finland (FiDiPro). He is the author of two textbooks and five general books. He has over 250 peer-reviewed journal articles.

Dr. Chandrasekar has served as a member of the National Academy of Sciences Committee that wrote the books on *Weather Radar Technology Beyond NEXRAD* and *Flash Flood Forecasting in Complex Terrain*. He is a fellow of the American Meteorological Society, URSI, and the National Oceanic and Atmospheric Administration (NOAA) Cooperative Institute for Research in the Atmosphere (CIRA). He was a recipient of numerous awards including the Knighthood by the Government of Finland, the NASA Technical Contribution Award, the NASA Group Achievement Award, the NASA Robert H. Goddard Exceptional Achievement Award, the Outstanding Advisor Award, the CSU Innovations Award, the IEEE GRSS Education Award, the NOAA/NWS Directors Medal of Excellence, and the IEEE GRSS Distinguished Achievement Award. He has served as the General Chair for the IEEE IGARSS'06 Symposium. He currently serves as the Chair for the Commission F and the International Union of Radio Science (URSI). He also served as a Chief Editor for the *Journal of Atmospheric and Oceanic Technology* and a Guest Editor for the IEEE TRANSACTIONS ON GEOSCIENCE AND REMOTE SENSING and the IEEE JOURNAL OF SELECTED TOPICS IN APPLIED EARTH OBSERVATIONS AND REMOTE SENSING.